Zinc Oxide Nanostructures: Morphology Derivation and Evolution

Changhui Ye,* Xiaosheng Fang, Yufeng Hao, Xuemei Teng, and Lide Zhang

Key Laboratory of Materials Physics, Institute of Solid State Physics, Chinese Academy of Sciences, and Graduate School of Chinese Academy of Sciences, Hefei 230031, P. R. China

Zinc oxide nanostructures of various types, including nanobelts, nanoplatelets, nanowires, and nanorods, have been synthesized via well-developed routes by many research groups. However, so far, the underlying mechanism for the morphology derivation and evolution of the nanostructures has not been elucidated in depth. In this article, we report the systematic investigation of the morphology evolution characteristics of ZnO nanostructures from dense rods to dense nanoplatelets, nanoplatelet flowers, dense nanobelt flowers, and nanowire flowers in an evaporation−physical transport−condensation approach. Through the use of crystal growth theory, the determining factors for the formation of different nanostructural morphologies were found to be gas-phase supersaturation and the surface energy of the growing surface planes. Other experimental parameters such as the temperature at the source and the substrate, the temperature difference and the distance between the source and the substrate, the heating rate of the furnace, the gas flow rate, the ceramic tube diameter, and the starting material are all correlated with supersaturation and impose an effect on the morphology evolution. This finding may have an important impact on the qualitative understanding of the morphology evolution of nanostructures and the achieving of desired nanostructures controllably.

Introduction

With the ongoing miniaturization of devices, the synthesis of low-dimensional building blocks including nanotubes, nanowires, nanorods, nanobelts, and nanoplatelets has attracted extensive research interest.[1] For the past decade, a wide variety of methods have been developed to synthesize many kinds of nanostructures, and many of the achievements have already been summarized in several review papers.[2] Among the methods, the evaporation−physical transport−condensation (EPTC) approach has demonstrated its versatility in obtaining a rich family of nanostructures superior to other methods. Recently, Wang's group has shown that an unprecedented rich family of ZnO nanostructures could be synthesized by this method.[3] Moreover, this method is the most efficient one to embody the intrinsic crystallography of the material into the nanostructures. There have been a wide variety of ZnO nanostructures appearing in recent years, including rods, wires, belts, tubes, cages, walls, spirals, rings, flowers, and so on.[4−9] However, for the building blocks to incorporate into functional nanodevices, the controlled synthesis of the nanostructures for desired size, shape, and orientation should be fulfilled first, which is a rather challenging issue and has made less progress owing to its toughness. This problem could be partially solved by trial and error; however, thorough understanding of the determining factors in the growth of nanostructures may settle down the uncertainty. Although some researchers have noticed this problem, and tried to explain the morphology variation with experimental parameters such as temperature, gas flow rate, and the distance between the source material and the substrate, the explanations are rather superficial and there have been many controversies over the influence of the experimental parameters on the morphology variation. Some preliminary results showed that with increasing temperature, the morphology evolved from nanowires to nano-

belts then to nanosheets; with the increase of gas flow rate, the size of the nanostructures increased, and with the increase of the distance between source material and the substrate, the size of the nanostructures decreased.[10] However, there were also results which showed the contrary trends in the case of GaN nanomaterials.[11] Therefore, the determining factors for the variation of the nanostructures should be elucidated to a first priority to realize the controlled synthesis of desired nanostructures and accelerate the progress in the fabrication of nanodevices.

It is generally believed that growth temperature and gas-phase supersaturation determine the growth rate of surface planes and the final morphology of the crystals, with other experimental parameters playing minor roles. In this article, by taking ZnO as an example, we report on the correlation of the experimental parameters including the temperature at the source material and the substrate, the temperature gradient in the tube furnace, the distance from the source material and the substrate, the heating rate of the furnace, the gas flow rate, the inner diameter of the ceramic tube, and the starting material in an EPTC process on influencing the growth of nanostructures with various morphologies. The choice of ZnO is based on two facts: On one hand, the morphology of ZnO has been proven to be the richest among inorganic semiconductors,[3] and thus the investigation of the morphology derivation and evolution of ZnO nanostructures could facilitate the understanding of crystal growth kinetics of other materials; on the other hand, ZnO is the most promising wide band gap inorganic semiconductor, and has significant applications in optoelectronics, photonics, sensors, and varistors.[12] The dominant factors for the derivation and evolution of the nanostructures were found to be the gas-phase supersaturation and the surface energy of the growing surface planes; namely, the gas-phase supersaturation of the atoms or molecules of the growing material determines the growth rate of the crystal, and the surface energy of the growing surface planes determines

* To whom correspondence should be addressed. E-mail: chye@issp.ac.cn.

Zinc Oxide Nanostructures

J. Phys. Chem. B, Vol. 109, No. 42, 2005 **19759**

the significance of which in the final crystal, with other parameters entering into the process by influencing the former parameters. This finding may have an important impact on the understanding of the morphology derivation and evolution of nanostructures and achieving of desired nanostructures controllably.

Experimental Section

Material Preparation. The experimental setup is a conventional horizontal tube furnace as described previously.[13] Commercial ZnO and graphite powders mixed in a molar ratio of 4:1 were placed in a ceramic boat and loaded into the central region of a ceramic tube (inner diameter 40 mm, length 70 cm). Several pieces of Si wafers were placed downstream in the tube side-by-side, and another Si wafer was put above the source materials horizontally, as the deposition substrates. The system was rapidly heated to 1050 °C in 12 min with the flow rate of the carrier gas (Ar) of 20 sccm and kept at this temperature for 90 min. Various ZnO nanostructures were deposited on Si substrates in a temperature range of 1050−750 °C.

Material Characterization. The collected products were characterized by scanning electron microscopy (SEM, JEOL JSM 6300), transmission electron microscopy (TEM, Hitachi 800), selected area electron diffraction (SAED), and high-resolution electron microscopy (HREM, JEOL2010).

Theoretical Basis. Crystal growth theories have been developed extensively during the last century. Growth of whiskers from the vapor through the EPTC process was known earlier and theoretically modeled by Burton, Cabrera, and Frank (BCF theorem)[14] and later elaborated by Sears et al.[15] This theory was based on the operation of a screw dislocation at the tip of the growing whiskers as the source of growth steps; however, many of the experimental results showed that the screw dislocations had not been universally experimentally confirmed and other defects such as dislocations, stacking faults, and twin crystals could also provide the growth steps.[16] It has been well-known that crystals grow at thermal equilibrium conditions to the final shape determined by Wulff theorem;[17] namely, the crystals are bound with surface planes of minimum total surface free energy. However, the growth of whiskers in reality takes place under nonequilibrium conditions; thus, the final morphology of the crystals may deviate greatly from what Wulff theorem predicts, which means that the growth behavior of various planes is manifested kinetically.

Burton et al.[14] investigated the growth of crystal planes under certain gas-phase supersaturation and found out that the density of kinks on a plane could be written as

$$\rho = \frac{1}{\lambda_0^2} \qquad (1)$$

where λ_0 is the mean spacing between kinks and can be further written as

$$\lambda_0 = \frac{1}{2} a \exp\left(\frac{\Delta G_{\text{kink}}}{k_B T}\right) \qquad (2)$$

where a is the distance of molecules along a certain step, ΔG_{kink} is the formation energy of a kink, k_B is Boltzmann's constant, and T is the absolute temperature. As for the (111) planes of a face-centered-cubic (fcc) structure, the estimation $\Delta G_{\text{kink}} \cong 0.5 \phi$ holds, where ϕ is the interaction energy between nearest neighbors. Generally speaking, ΔG_{kink} is larger for low-indexed, closely packed planes than for high-indexed, sparsely arranged

planes, which implies that the sparser the plane packing, the larger the kink density in that plane and vice versa.

When a gas molecule impinges on a plane, it will condense readily with the condensation efficiency close to unity.[18] If the molecule could find an energetically favorable site (most probably a kink) after diffusion jumps prior to desorption into the gas phase, then it will have a good chance to incorporate into the crystal lattice where this plane will grow. It is apparent that a plane with high kink density will possess a high incorporation efficiency of the adsorbed molecules. It was also shown by Burton et al.[14] that the foot-mean-square diffusion distance of a molecule on a plane was given by

$$\lambda_s = \sqrt{2D\tau} \cong a_D \exp\left(\frac{\Delta G_{\text{des}} - \Delta G_{\text{diff}}}{2k_B T}\right) \qquad (3)$$

where D is the diffusion coefficient, τ is the mean stay time of an adsorbed molecule before desorption into the vapor, a_D is the diffusion jump distance, and ΔG_{des} and ΔG_{diff} are the activation energies for desorption and surface diffusion, respectively. It also holds that $\Delta G_{\text{diff}} \cong 0.1 \Delta G_{\text{des}}$ and $\Delta G_{\text{des}} \cong 5/6 \Delta H_{\text{evap}}$, with ΔH_{evap} the evaporation enthalpy.[19] Then, formula 3 can be rewritten as

$$\lambda_s \cong a_D \exp\left(\frac{\Delta H_{\text{evap}}}{2.64 k_B T}\right) \qquad (4)$$

Thus, the diffusion distance is smaller for a low-indexed, closely packed plane with lower free energy. For example, Burton et al.[14] showed that for a (100) surface plane in a fcc crystal, the diffusion distance is about 1 order larger than that of a closely packed (111) surface plane. Together with the kink density formulation discussed above, it is natural to draw the conclusion that the higher the free energy of a plane, the faster the growth velocity of it.

By solving continuity partial differential equations under certain boundary conditions, Ruth et al. derived the kinetic characteristics of diffusion-controlled whisker growth.[20] It was demonstrated that the whiskers followed an exponential growth law in the initial stage and when the length of the whiskers approached λ_s, the growth changed to a linear law. The time-dependent length of the whiskers in the initial stage can be simply written as

$$h(t) = h_0 \exp(\gamma t) \qquad (5)$$

with

$$\gamma = \frac{p - p_0}{r\rho} \sqrt{\frac{2m}{\pi k_B T}} = \frac{S p_0}{r\rho} \sqrt{\frac{2m}{\pi k_B T}} \qquad (6)$$

where h_0 is a constant, r is the radius of the whiskers, ρ is the density of the whiskers, p and p_0 are the real gas-phase pressure and the equilibrium pressure with an infinite flat surface, and S is the gas-phase supersaturation, defined by

$$S = \frac{p - p_0}{p_0} \qquad (7)$$

When the length of the whiskers is smaller than the diffusion distance, all the impinged molecules have a chance to be captured by the growing tip of the whiskers, and thus, the whiskers will lengthen rather than thicken; however, when the length of the whiskers is approaching the diffusion distance, a fraction of the impinged molecules on the base of the whiskers

will have a chance to desorb from the surface, or if the supersaturation is very high, then two-dimensional (2D) nucleation on the base of the whiskers may take place and the whiskers will thicken. Sears[15] has given the nucleation rate as

$$\dot{N} = B \exp\left(-\frac{\Delta f}{k_B T}\right) \tag{8}$$

with the free energy for the formation of a critical-sized surface nucleus Δf defined by

$$\Delta f = \frac{\pi a \sigma^2 m}{\rho k_B T \ln(S + 1)} \tag{9}$$

where B is a constant, a the interlayer spacing for the growing plane, σ the surface free energy of the step created, and m the atomic weight. From eqs 8 and 9, it is straightforward that 2D nucleation could be initiated with large supersaturation, especially for those surface planes on which the free energy of the formed steps is small, for example, the high-indexed planes.

The formulation in the previous sections could be readily extended for morphologies other than whiskers, for example, belt, platelet, and sheet. The competition of capture of the impinged molecules by different surface planes under certain supersaturation determines the final morphology of the following structures: nanowires, nanorods, nanobelts, or nanoplatelets.

Results

The morphologies of ZnO nanostructures vary with the distance from the source material to the substrate from dense rods to dense nanoplatelets, nanoplatelet flowers, dense nanobelt flowers, and nanowire flowers with each morphology happening in a wide region and in high yield. The morphology of the structure on the substrate above the source material is displayed in Figure 1a, where the structure forms a dense filmlike layer with areas covering over 1 cm². The high magnification image in Figure 1b reveals that the film is composed of a high density of ZnO rods with diameter of several micrometers and length of tens of micrometers. The rods form arrays with nearly parallel orientation perpendicular to the substrate. It is noteworthy that the rods are faceted, both for the side planes and for the growing tips. In the downstream side of the source material, the substrate most adjacent to the source material was covered with a dense filmlike layer with areas extending to several centimeter squares as shown in Figure 1c. The high magnification image of the nanostructure is displayed in Figure 1d, where the high density of nanoplatelets with random orientation are exhibited. The nanoplatelets generally have length of about 10 μm, width of 1−2 μm, and thickness of tens of nanometers. With the increase in distance between the source material and the substrate, the density of the nanoplatelets decreases and a flowerlike ensemble of nanoplatelets forms on the substrate, which is displayed in Figure 1e. The high magnification image in Figure 1f reveals that the nanoplatelets grew from the same location and had dimensions a little bit smaller than those in the former region, with the shape being similar. With the further increase in distance between the source material and the substrate, the morphology of the nanostructures changes to a high density of flowerlike nanobelt bundles and this region covers several millimeters along the temperature gradient direction. As shown in Figure 1g, the nanowires seem to initiate from separate centers, outgrow radially, and form networks. The high magnification image in Figure 1h exhibits bending and twisting of the long nanobelts whose length extends to several tens of
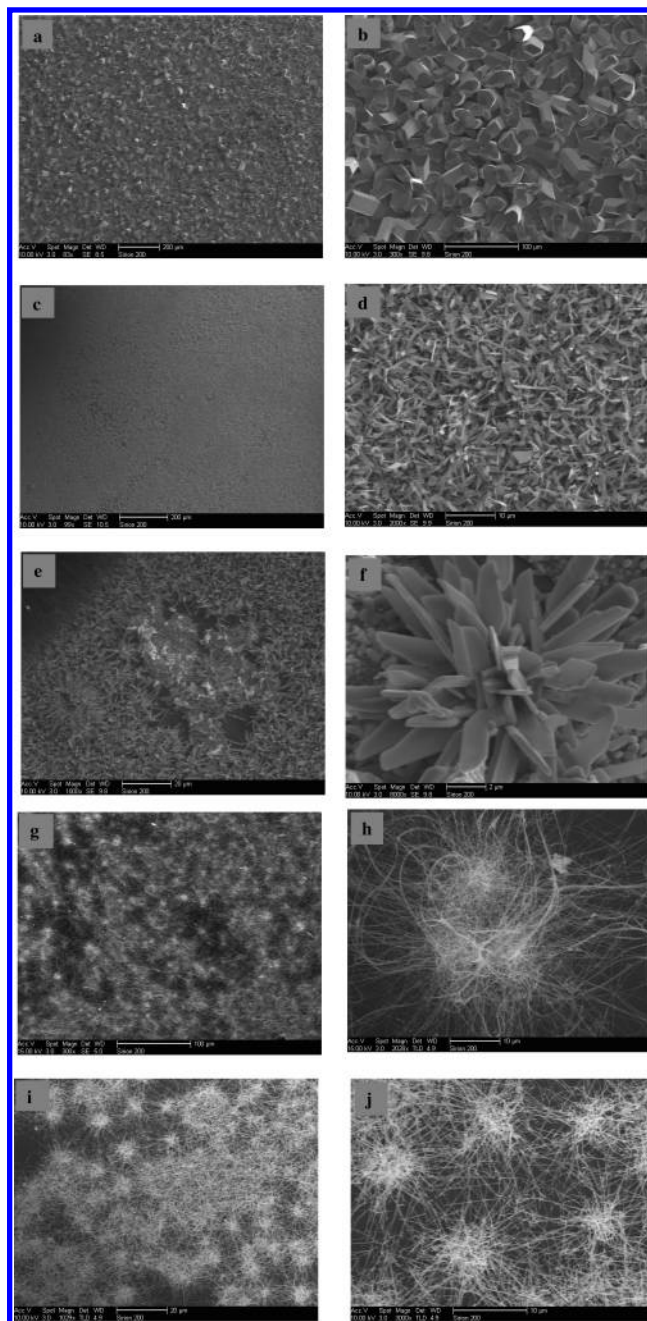

Figure 1. Typical SEM images of morphologies of ZnO structures: dense filmlike rods (a), dense filmlike nanoplatelets (c), flowerlike nanoplatelets (e), nanobelts (g), and nanowires (i). The corresponding high magnification views are displayed in (b), (d), (f), (h), and (j), respectively.

micrometers and width of tens of nanometers. When the distance between the source material and the substrate increases further, the nanobelts transform to nanowires, while retaining the flowerlike bundles grown from separate centers. This region covers several centimeter squares, with the density of the flowers decreasing upon the increase in distance between the source material and the substrate. Parts i and j of Figure 1 exhibit the low and high magnification SEM image of the flower bundles of the ZnO nanowires. The nanowires have a length of more than 10 μm and diameter of several tens of nanometers.

It is noteworthy that the aspect ratio (defined by length divided by width for nanoplatelets and nanobelts and length divided by diameter for rods and nanowires) of the structures increases with the increase in distance from the source material
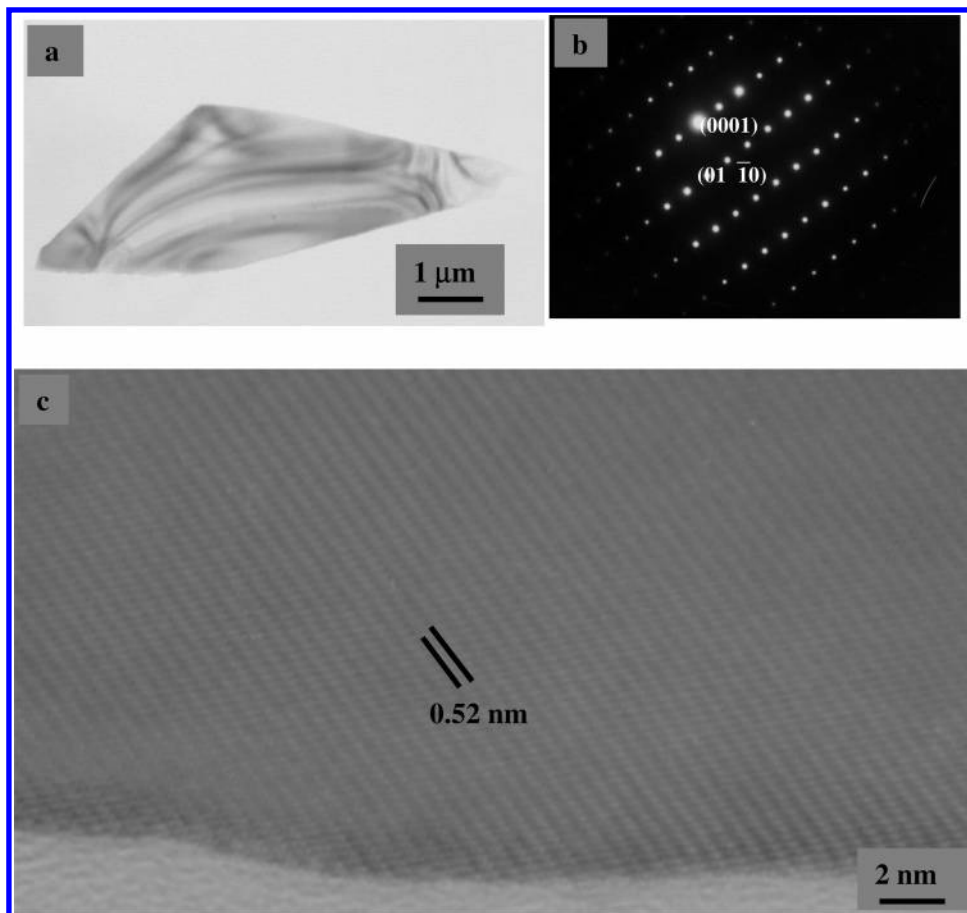
Figure 2. (a) Typical TEM image of a ZnO nanoplatelet, which is irregular in shape. (b) SAED pattern taken along the $\langle 2\bar{1}\bar{1}0 \rangle$ zone axis. (c) HRTEM image of the nanoplatelet.

to the substrate, with <5 for rods, 5–10 for nanoplatelets, 10–500 for nanobelts, and >500 for nanowires.

The structures of the materials have also been investigated by employing TEM and HRTEM. Characteristic structural analyses are displayed in Figures 2–4 . The ZnO rods obtained above the source material are too thick to image under TEM, therefore, only nanoplatelets, nanobelts, and nanowires are exhibited. In Figure 2a, a ZnO nanoplatelet is shown, which is irregular in shape with rough surfaces. The surface planes do not seem to correspond to any low-indexed planes. The SAED pattern in Figure 2b taken along the $\langle 2\bar{1}\bar{1}0 \rangle$ zone axis reveals that although the nanoplatelet does not show any preferred growth directions, the top and bottom surfaces are fixed as $\pm(2\bar{1}\bar{1}0)$ planes. Figure 2c displays the HRTEM image of the nanoplatelet, where the lattice planes with a spacing of 0.52 nm correspond to the (0001) planes. Different from the nanoplatelets, the nanobelts possess well-defined shapes similar to those Wang et al. reported.[9] The typical morphologies of the nanobelts are shown in Figure 3a, where some of the nanobelts show decreasing width from the base to the tip. The dark lines are bending contours that are common to nanobelts.[9] The nanobelts are about 100 nm in width and several tens of micrometers in length. The same as for the nanoplatelet, the SAED pattern in Figure 3b taken along the $\langle 2\bar{1}\bar{1}0 \rangle$ zone axis also means that the nanobelt has $\pm(2\bar{1}\bar{1}0)$ top and bottom surfaces. Different from the former, the latter has fixed growth directions, namely, the fastest growth direction is along the [0001] axis and the second fastest one along [01$\bar{1}$0]. Therefore, on the basis of the TEM image and the SAED pattern, the side surfaces can be assigned as $\pm(01\bar{1}0)$ planes and the tip and base surfaces can be assigned as $\pm(0001)$ planes. The HRTEM image

in Figure 3c shows well-defined 2D lattice planes and demonstrates the good crystallinity of the nanobelts. The lattice planes with spacings of 0.52 and 0.28 nm correspond to the (0001) and (01$\bar{1}$0) planes, respectively. Nanowires of ZnO in the present work generally have diameters smaller than 50 nm and lengths of several tens of micrometers. A ZnO nanowire with diameter of about 30 nm is displayed in Figure 4a, and it also shows tapering to a small extent along the length. The SAED pattern of the nanowire in Figure 4b taken along the $\langle 2\bar{1}\bar{1}0 \rangle$ zone axis shows the same rectangular diffraction pattern as that of the nanobelts. The nanowire also has the [0001] axis as its growth direction. From the HRTEM image in Figure 4c, well-defined 2D lattice planes corresponding to (0001) and (01$\bar{1}$0) planes are also observed. Steps and roughness have been found on the surface of the nanowire and are marked with arrows.

Discussion

The experimental parameters that determine or influence the morphology derivation and evolution of the ZnO nanostructures include the gas-phase supersaturation, the surface energy of the growing surface planes, the temperature at the source material and the substrate, temperature gradient in the tube furnace, the distance from the source material and the substrate, the heating rate of the furnace, the gas flow rate, the inner diameter of the ceramic tube, and the starting material. Their roles in the formation of various morphologies are analyzed in the following sections.

Supersaturation and Surface Energy. The growth theories and technologies of crystals both for perfect large size ones or for films have been well documented; however, the parameter
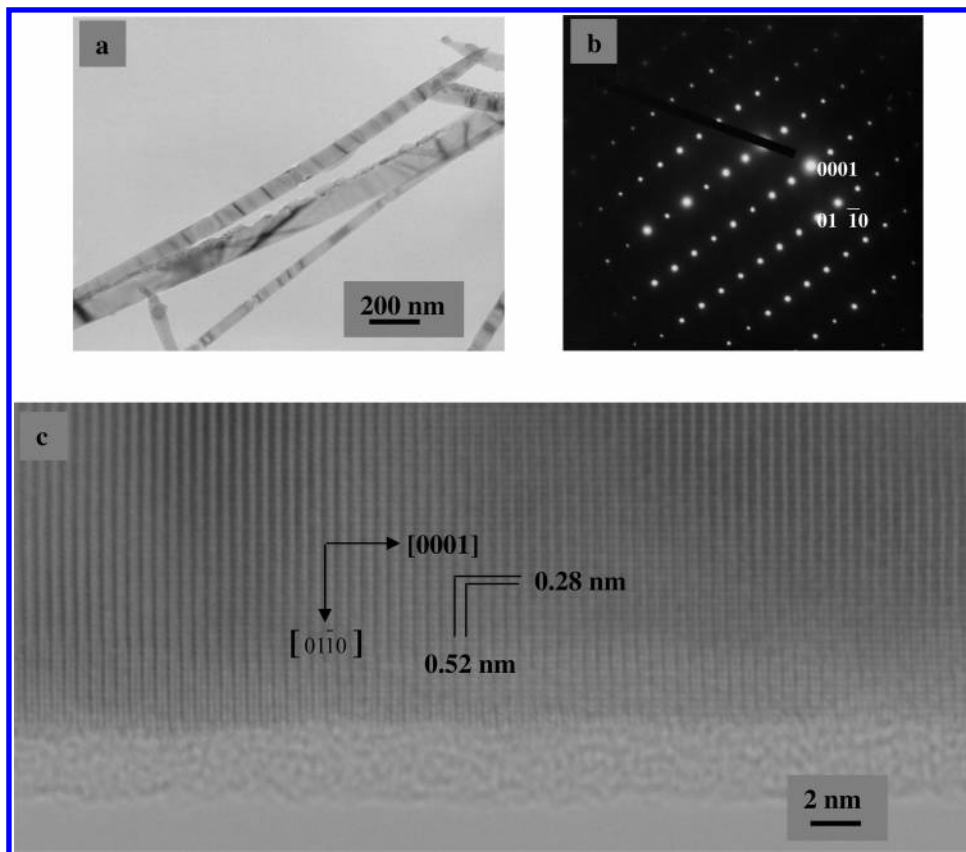
Figure 3. (a) Typical TEM image of ZnO nanobelts, some of which show the tapering in width along the length. (b) SAED pattern taken along the $\langle 2\bar{1}\bar{1}0\rangle$ zone axis. (c) HRTEM image of a nanobelt with the length along [0001] and width along [01$\bar{1}$0] directions, respectively.

window for either form is relatively narrow, therefore, they are not able to extend to the growth of nanoscale nanostructures. For example, growth of bulk size perfect crystals is always carried out under a very low gas-phase supersaturation, namely, *S* is close to zero. Under this circumstance, the crystal grows at near thermal equilibrium conditions and the shape of the crystal is well defined by Wulff theorem and reflects the internal crystallography of the crystal itself.[17,21] In an effort to grow nanoscale structures, such as nanoplatelets, nanobelts, nanowires, and nanorods, the supersaturation is generally much larger than the unity and the crystal grows under conditions far away from thermal equilibrium. Under such a circumstance, growth kinetics takes a part or even determines the growth behavior of the surface planes and the final morphology of the structure.

Similar to what Brenner[22] and Nam et al.[11] proposed, the forced diffusion of vapor by a carrier gas is more important than the molecular diffusion driven by a concentration gradient for the low Reynolds number of our system. Under this advection condition, there generally exists a maximum in the ZnO vapor concentration and the supersaturation downstream from the source material, and as the flow rate of the Ar carrier gas increases, the maximum shifts further downstream, as qualitatively illustrated in Figure 5. In the heating process, ZnO powders were reduced partially by graphite (a ratio of 4:1 for ZnO to C was used to reduce ZnO partially to form gaseous zinc suboxide) and zinc suboxide vapor formed (carbon dioxide may also form in the reaction). In the transportation from the source region to the substrate, the zinc suboxide vapor may be oxidized by residual oxygen or the carbon dioxide in the furnace.

In region I, the supersaturation is low and rods with well-defined facets of the $\{10\bar{1}0\}$ major plane, $\{01\bar{1}1\}$ capping planes, (000$\bar{1}$) base plane, and (0001) minor tip plane are formed similar to those of Laudise et al.[23] and Baxter et al.[24] The crystal

growth in this region best reflects the crystallographic symmetry of the hexagonal ZnO. In Figure 6, it is noticed that some rods possess the (0001) minor planes, while others have no (0001) surface planes at all. However, the shape of the rods is still similar, which also means that kinetic factors play a minor role in the present case, and the morphology of the ZnO rods is a reflection of the ideal hexagonal structure.[24]

At region II, the supersaturation is the highest, where the growth behavior of the structure is quite different from that in region I. The growth takes place under circumstances far from thermal equilibrium, and the kinetics plays a more significant role in determining the morphology of the structure. As illustrated in Figure 7, when a molecule is adsorbed on a surface plane, for example, the top surface of a plate shaped structure, it will undergo four processes: diffusing to the front surface plane (F), the side surface plane (S), and on the top surface plane (T) and incorporating into lattices, thus desorbing away from the surfaces. When the top surface is the lowest in surface energy, according to the Theoretical Basis section, the diffusion distance is the smallest for the molecules adsorbed on this surface and thus, the molecules have little chance to incorporate into the lattice plane on this surface. Meanwhile, the molecules have a good chance to diffuse to the front and the side surfaces, where the surface energies are higher and diffusion distances are longer; thus, the molecules are much easier to incorporate into the lattice planes on these surfaces. This case was interpreted as kinetic roughness earlier.[25] Furthermore, it should be kept in mind that the higher the surface energy, the easier the nucleation on that surface. There is also a positive feedback effect in this competition process, namely, the more aggressive the competition for capturing the adsorbed molecules, the faster the growth rate for the front and side surfaces and then the larger the surface area for the top surface; thus, the larger the area for
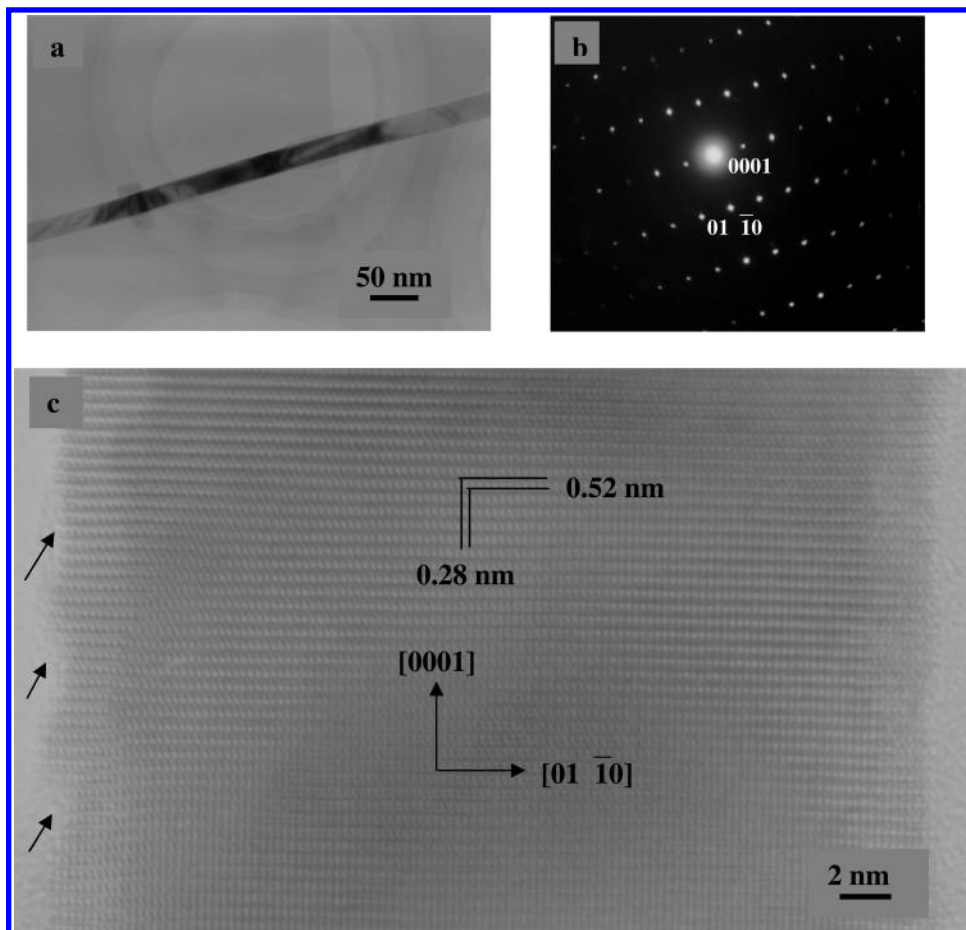
Zinc Oxide Nanostructures

J. Phys. Chem. B, Vol. 109, No. 42, 2005 **19763**

Figure 4. (a) Typical TEM image of a ZnO nanowire, which is about 30 nm in diameter and shows a little tapering along the length. (b) SAED pattern taken along the $\langle 2\bar{1}\bar{1}0 \rangle$ zone axis. (c) HRTEM image of the nanowire. Steps are observed on the edge of the nanowire and marked with arrows.
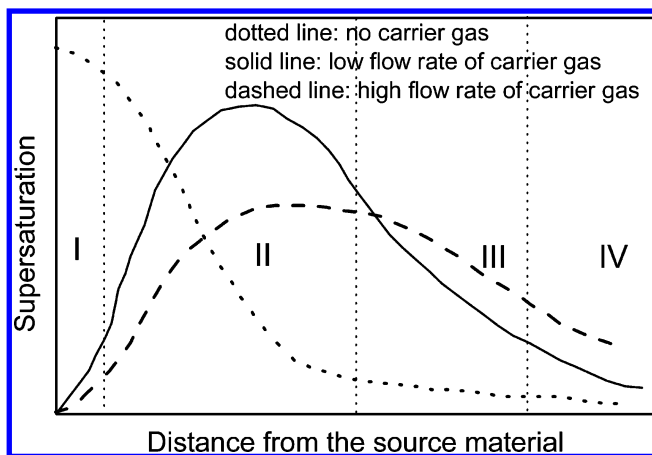

Figure 5. Qualitative supersaturation profile of ZnO vapor in the reactor under a different flow rate of carrier gas along the distance downstream from the source material. Regions I, II, III, and IV correspond to microrods, nanoplatelets, nanobelts, and nanowires, respectively, with a low flow rate of carrier gas.

Figure 6. SEM image of hexagonally shaped ZnO rods. The insets show rods with a small and complete disappearance of the (0001) minor surface plane, respectively.

the top surface, the larger the collection number of impinged molecules on this surface there will be to support the growth of the front and side surfaces. Failure to capture the adsorbed molecules leads to the much slower growth of the top surface. The aggressive characteristics of the front and the side surfaces similarly determine their proportion in the final morphology. When these two surfaces are similar in surface energy or belong to the same family of lattice planes, the competitive ability of these surfaces is also simila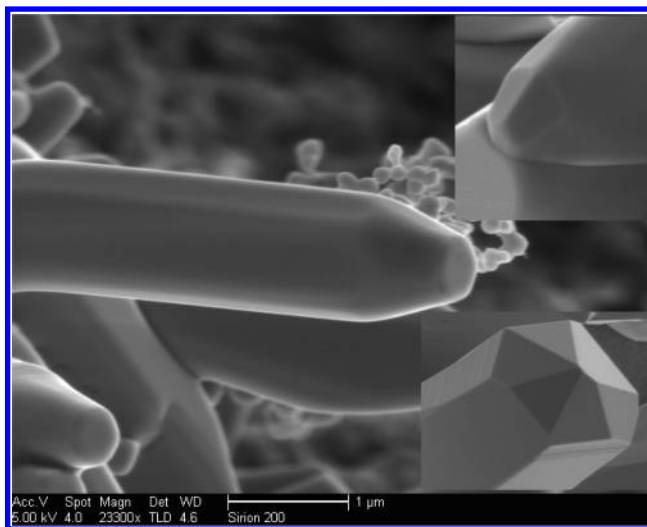r. Then, the morphology may take the form of a nanosheet or a nanoplatelet structure. On the contrary, when these two surfaces differ greatly in energy, the final morphology may be more like a nanobelt as in region III, where the supersaturation is lower than that in region II and the competitive capturing of the adsorbed molecules is more severe, namely, the front surface captures the molecules not only from the top surface but also from the side surface. When the crystal has several fast growth directions, for example, ZnO
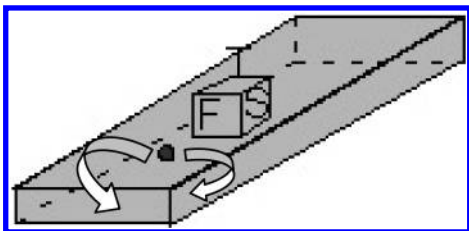
Figure 7. Schematic drawing illustrating the competition of capturing the adsorbed molecules.
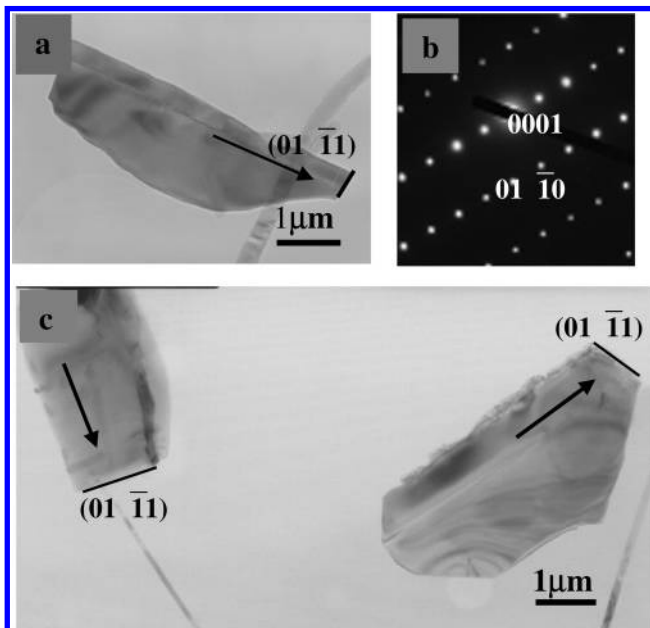

Figure 8. SEM images of irregularly shaped ZnO nanoplatelets growing along the polar (01$\bar{1}$1) planes (a) and (c). (b) SAED pattern of the nanoplatelet in (a).

Figure 9. Pressure profile as a function of temperature for ZnO.

of the Furnace. The temperature at the source material determines the vapor pressure of it, and the temperature-dependent pressure profile of ZnO[26] is shown in Figure 9. The pressure increases exponentially with heating temperature. When the vapor advects within the carrier gas downstream to the substrates, there will be a build up of local supersaturation higher than that in the case with lower heating temperature. Therefore, the morphology will change accordingly. The temperature at the substrate and the temperature gradient similarly influence the supersaturation profile and hence the morphology. Distance from the source material and the substate implies the selection of a local supersaturation and temperature. The heating rate may have an influence on the initial nucleation process: A higher heating rate makes the homogeneous nucleation and low dispersity of the morphology possible, while a lower heating rate generally causes high dispersity.

Temperature at the substrate has another effect on the crystal growth: Higher temperatures at regions I and II favor the high-density, homogeneous nucleation, therefore, the large area, filmlike structure as demonstrated in parts a and c of Figure 1; lower temperatures at regions III and IV facilitate the formation of low-density, inhomogeneous nucleation of large polycrystals and the following recrystallization and growth of flowerlike structures as displayed in parts f, h, and j of Figure 1.

Gas Flow Rate and Inner Diameter of the Ceramic Tube. The gas flow rate and the inner diameter of the ceramic tube have a fundamental influence on the supersaturation profile through the interaction with the Reynolds number. In Figure 5, the supersaturation profile under a different gas flow rate has been displayed. With a higher gas flow rate and smaller inner diameter of the ceramic tube, the maximum supersaturation will move downstream from the source material and the morphology of the structure at a fixed position on the substrate will change accordingly.

Starting Material. Materials with nanometer-scaled sizes have been well-known to show a decrease in melting temperature.[27] Therefore, the use of nanomaterial as the source corresponds to elevating the heating temperature of the source material and similarly changes the supersaturation profile and the final morphology of the structure.

There are also other factors which may have an influence on the morphology in a particular circumstance, such as the addition of surfactant and mineralization agent; however, they are not pertinent to the present study and will be discussed in another paper.

shows the fast growth directions along the [0001], [2$\bar{1}\bar{1}$0], and [01$\bar{1}$0] axes and has polar surfaces of (0001) and (01$\bar{1}$1),[9] the morphology of the nanoplatelets is generally irregular as exhibited in Figure 8. Although the nanoplatelets are irregular in shape, they show the preferred growth direction along the packing of the polar (01$\bar{1}$1) planes. It is also interesting that these nanoplatelets have the same SAED pattern to that of the nanobelts shown in Figure 3b, which simply means that the nanoplatelets also have top and bottom surfaces of ±(2$\bar{1}\bar{1}$0). When the substrate is far away from the source material, then the supersaturation is very low. The competition is more severe for the adsorbed molecules than in region III, the morphology develops its quasi-one-dimensional character and nanowires are formed. The aspect ratio also increases through region I to region IV. The tapering of the nanowires and nanobelts implies the overgrowth of the structure with the length approaching the diffusion distance.

It is also noteworthy that under the kinetics-controlled growth of the nanostructures in regions II−IV, the thermodynamics still plays a role in influencing the final morphology, namely, the Wulff theorem partially holds in these circumstances. For the ZnO nanoplatelets, nanobelts, and nanowires, the surfaces with the lowest energy such as the {2$\bar{1}\bar{1}$0} family maximize in area, those with high energy such as the (0001) planes minimize in area, and those with very high energy and high indexes diminish completely in the final morphology.

Temperature at the Source Material and the Substrate, Temperature Gradient in the Tube Furnace, Distance from the Source Material and the Substrate, and Heating Rate
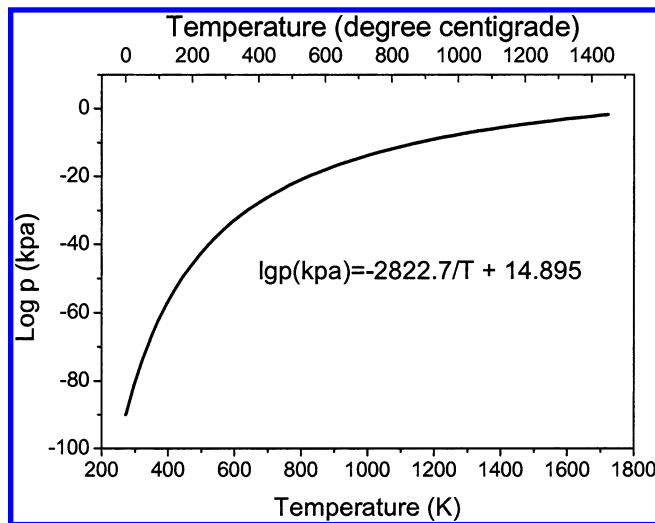
A crystal that grows through the EPTC technique is able to manifest its internal crystallographic symmetry, with the consideration of the lattice structures of the crystal and proper control of the experimental parameters; desired morphologies including nanobelts, nanoplatelets, nanowires, and nanorods could be obtained reproducibly. However, although the theoretical explanations for the morphology derivation and evolution proposed in this article could successfully account for the experimental phenomena observed by us and many researchers, they are not theoretically rigorous. It is far more complex for those molecules with ionic or valent character to incorporate into the crystal lattice considering that not all the available kink sites could be used due to the restraint of the coodination number and the valence angle for a specific crystal structure. It should be pointed out that the theoretical modeling of the initial nucleation of the crystal nucleus and the details of the diffusion jump processes of adsorbed molecules should be carried out using molecular dynamics simulations or ab initio calculations to gain more insights into the growth of various forms of nanostructures.

Conclusions

In summary, we have investigated the morphology derivation and evolution of ZnO nanostructures and elucidated the underlying mechanism responsible for the variation of the structures. The gas-phase supersaturation determines the growth rate of the structure, and the surface energy of a plane under certain supersaturation decides its activity: growth rate and the proportion in the final structure. Other experimental parameters, such as the temperature of the source material and the substrate, the temperature gradient in the tube furnace, the distance from the source material and the substrate, the gas flow rate, the inner diameter of the ceramic tube, and the starting material, all play a role in influencing the final morphology of the structure by entering into the supersaturation term. The competition of the capture of impinged molecules by different surface planes under certain supersaturation determines the final morphology of the following structures: nanowires, nanorods, nanobelts, or nanoplatelets. Generally speaking, very low supersaturation favors the growth of perfect crystals with the internal symmetry, modestly low supersaturation benefits the formation of nanowires, medium supersaturation facilitates the growth of nanobelts, moderately high supersaturation tends toward the formation of nanoplatelets, nanosheets, and continuous films, and very high supersaturation causes the rapid formation of poorly crystallized crystals with undefined morphology. This finding may have an important impact on understanding the morphology evolution of nanostructures and achieving desired nanostructures controllably.

References and Notes

(1) Lauhon, L. J.; Gudiksen, M. S.; Wang D.; Lieber, C. M. *Nature* **2002**, *420*, 57−61. (b) Cui, Y.; Lieber, C. M. *Science* **2001**, *291*, 851−853. (c) Zhu, T. C.; Bando, Y.; Xue, D. F.; Golberg, D. *J. Am. Chem. Soc.* **2003**, *125*, 16196−16197. (d) Gao, Y. H.; Bando, Y. *Nature* **2002**, *415*, 599−599.

(2) Yang, P.; Yan, H.; Mao, S.; Russo, R.; Johnson, J.; Saykally, R.; Morris, N.; Pham, J.; He, R.; Choi, H. *Adv. Funct. Mater.* **2002**, *12*, 323−331. (b) Dai, Z. R.; Pan, Z. W.; Wang, Z. L. *Adv. Funct. Mater.* **2003**, *13*, 9−24. (c) Rao, C. N. R.; Deepak, F. L.; Gundiah, G.; Govindaraj, A. *Prog.*

Solid State Chem. **2003**, *31*, 5−147. (d) Wang, Z. L. *Annu. Rev. Phys. Chem.* **2004**, *55*, 159−196. (e) Law, M.; Goldberger, J.; Yang, P. *Annu. Rev. Mater. Res.* **2004**, *34*, 83−122. (f) Xia, Y.; Yang, P.; Sun, Y.; Wu, Y.; Mayers, B.; Gates, B.; Yin, Y.; Kim, F.; Yan, H. *Adv. Mater.* **2003**, *15*, 353−389.

(3) Wang, Z. L.; Kong, X. Y.; Ding, Y.; Gao, P.; Hughes, W. L.; Yang, R.; Zhang, Y. *Adv. Funct. Mater.* **2004**, *14*, 943−956. (b) Wang, Z. L. *J. Phys.: Condens. Matter* **2004**, *16*, R829−R858.

(4) Pan, Z. W.; Dai, Z. R.; Wang, Z. L. *Science* **2001**, *291*, 1947−1949. (b) Hu, J. Q.; Bando, Y.; Zhan, J. H.; Li, Y. B.; Sekiguchi, T. *Appl. Phys. Lett.* **2003**, *83*, 4414−4416. (c) Chen, S.; Liu, Y.; Shao, C.; Mu, R.; Lu, Y.; Zhang, J.; Shen, D.; Fan, X. *Adv. Mater.* **2005**, *17*, 586−590.

(5) Tian, Z. R.; Voigt, J. A.; Liu, J.; Mckenzie, B.; Mcdermott, M. J.; Rodriguez, M. A.; Konishi, H.; Xu, H. *Nat. Mater.* **2003**, *2*, 281−286. (b) Chen, A. C.; Peng, X. S.; Koczkur, K.; Miller, B. *Chem. Commun.* **2004**, 1964−1965. (c) Tian, Z. R.; Voigt, J. A.; Liu, J.; Mckenzie, B.; Mcdermott, M. J. *J. Am. Chem. Soc.* **2002**, *124*, 12954−12955. (d) Wu, J. J.; Liu, S. C. *Adv. Mater.* **2002**, *14*, 215−218.

(6) Lao, J. Y.; Wen, J. G.; Ren, Z. F. *Nano Lett.* **2002**, *2*, 1287−1291. (b) Lao, J. Y.; Huang, J. Y.; Wang, D. Z.; Ren, Z. F. *J. Mater. Chem.* **2004**, *14*, 770−773.

(7) Lyu, S. G.; Zhang, Y.; Ruh, H.; Lee, H. J.; Shim, H. W.; Suh, E. K.; Lee, G. J. *Chem. Phys. Lett.* **2002**, *363*, 134−138. (b) Xing, Y. J.; Xi, Z. H.; Xue, Z. Q.; Zhang, X. D.; Song, J. H.; Wang, R. M.; Xu, J.; Song, Y.; Zhang, S. L.; Yu, D. P. *Appl. Phys. Lett.* **2003**, *83*, 1689−1691. (c) Roy, V. A. L.; Djurisic, A. B.; Chan, W. K.; Gao, J.; Lui, H. F.; Surya, C. *Appl. Phys. Lett.* **2003**, *83*, 141−143.

(8) Mo, M. S.; Yu, J. C.; Zhang, L. Z.; Li, S. A. *Adv. Mater.* **2005**, *17*, 756−760. (b) Hu, J. Q.; Li, Q.; Meng, X. M.; Lee, C. S.; Lee, S. T. *Chem. Mater.* **2003**, *15*, 305−308. (c) Pan, Z. W.; Mahurin, S. M.; Dai, S.; Lowndes, D. H. *Nano Lett.* **2005**, *5*, 723−727.

(9) Ng, H. T.; Li, J.; Smith, M. K.; Nguyen, P.; Gassell, A.; Han, J.; Meyyappan, M. *Science* **2003**, *300*, 1249−1249. (b) Zhang, B. P.; Wakatsuki, K.; Binh, N. T.; Segawa, Y.; Usami, N. *J. Appl. Phys.* **2004**, *96*, 340−343.

(10) Liao, L.; Li, J. C.; Liu, D. H.; Liu, C.; Wang, D. F.; Song, W. Z.; Fu, Q. *Appl. Phys. Lett.* **2005**, *86*, 083106. (b) Chen, C. C.; Yeh, C. C.; Chen, C. H.; Yu, M. Y.; Liu, H. L.; Wu, J. J.; Chen, K. H.; Chen, L. C.; Peng, J. Y.; Chen, Y. F. *J. Am. Chem. Soc.* **2001**, *123*, 2791−2798. (c) Wen, X. G.; Wang, S. H.; Ding, Y.; Wang, Z. L.; Yang, S. H. *J. Phys. Chem. B* **2005**, *109*, 215−220. (d) Fang, X. S.; Ye, C. H.; Zhang, L. D.; Wang, Y. H.; Wu, Y. C., *Adv. Funct. Mater.* **2005**, *15*, 63−68.

(11) Nam, C. Y.; Tham, D.; Fischer, J. E. *Appl. Phys. Lett.* **2004**, *85*, 5676−5678.

(12) Huang, M.; Mao, S.; Feick, H.; Yan, H.; Wu, Y.; Kind, H.; Weber, E.; Russo, R.; Yang, P. *Science* **2001**, *292*, 1897−1899. (b) Choy, J. H.; Jang, E. S.; Won, J. H.; Chung, J. H.; Jang, D. J.; Kim, Y. W. *Adv. Mater.* **2003**, *15*, 1911−1914. (c) Govender, K.; Boyle, D. S.; O'Brian, P.; Binks, B.; West, D.; Coleman, D. *Adv. Mater.* **2002**, *14*, 1221−1224. (d) Vayssieres, L. *Adv. Mater.* **2003**, *15*, 464−467.

(13) Ye, C. H.; Meng, G. W.; Jiang, Z.; Wang, Y. H.; Wang, G. Z.; Zhang, L. D. *J. Am. Chem. Soc.* **2002**, *124*, 15180−15181. (b) Ye, C. H.; Zhang, L. D.; Fang, X. S.; Wang, Y. H.; Yan, P.; Zhao, J. W. *Adv. Mater.* **2004**, *16*, 1019−1023. (c) Ye, C. H.; Meng, G. W.; Wang, Y. H.; Jiang, Z.; Zhang, L. D., *J. Phys. Chem. B* **2002**, *106*, 10338−10341.

(14) Burton, W. K.; Cabrera, N.; Frank, F. C. *Nature* **1949**, *163*, 398−399. (b) Burton, W. K.; Cabrera, N.; Frank, F. C. *Philos. Trans. R. Soc. London, Ser. A* **1951**, *243*, 299−358.

(15) Sears, G. W. *Acta Metall.* **1955**, *3*, 361−366. (b) Sears, G. W. *Acta Metall.* **1955**, *3*, 367−369. (c) Coleman, R. V.; Sears, G. W. *Acta Metall.* **1957**, *5*, 131−136. (d) Parker, R. L. *J. Chem. Phys.* **1962**, *37*, 1600−1605. (e) Blakely, J. M.; Jackson, K. A. *J. Chem. Phys.* **1962**, *37*, 428−430.

(16) Webb, W. W. *J. Appl. Phys.* **1958**, *29*, 817−820. (b) Drum, C. M.; Mitchell, J. W. *Appl. Phys. Lett.* **1964**, *4*, 164−165. (c) Ming, N. B. *J. Synth. Cryst.* **1992**, *21*, 217−222. (d) Takeuchi, S.; Iwanaga, H.; Fujii, M. *Philos. Mag. A* **1994**, *69*, 1125−1129.

(17) Herring, C. *Phys. Rev.* **1951**, *82*, 87−93.

(18) Hirth, J. P.; Pound, G. M. *J. Phys. Chem.* **1960**, *64*, 619−626.

(19) Sears, G. W. *J. Chem. Phys.* **1956**, *25*, 154−159.

(20) Ruth, V.; Hirth, J. P. *J. Chem. Phys.* **1964**, *41*, 3139−3149.

(21) Kaldis, E. *J. Cryst. Growth* **1969**, *5*, 376−390.

(22) Brenner, S. S. *Acta Metall.* **1956**, *4*, 62−74.

(23) Laudise, R. A.; Ballman, A. A. *J. Phys. Chem.* **1960**, *64*, 688−691.

(24) Baxter, J. B.; Wu, F.; Aydil, E. S. *Appl. Phys. Lett.* **2003**, *83*, 3797−3799.

(25) Givargizov, E. I. *J. Cryst. Growth* **1973**, *20*, 217−226.

(26) Xiang, S.; Yang, X.; Cao, T. In *Inorganic Chemistry Series* (in Chinese); Scientific Press: 2000; Vol. 6, p 717.

(27) Schmidt, M.; Kusche, R.; von Issendorff, B.; Haberland, H. *Nature* **1998**, *393*, 238−240. (b) Cleveland, C. L.; Luedtke, W. D.; Landman, U. *Phys. Rev. Lett.* **1998**, *81*, 2036−2039.